Journal of Materials Chemistry A

ROYAL SOCIETY OF CHEMISTRY

PAPER

View Article Online
View Journal | View Issue

Check for updates

Cite this: J. Mater. Chem. A, 2025, 13, 42343

Effect of nitrogen content on performance of supercapacitors composed of nitrogen–carbon materials

Mamta Devi, † Jyoti Shikhar† and Swati Sharma *

Received 10th August 2025
Accepted 5th November 2025

DOI: 10.1039/d5ta06469d

rsc.li/materials-a

Nitrogen–carbon (N–C) materials are emerging as an alternative to elemental carbon in advanced energy applications. Here we have established a correlation between the nitrogen content and supercapacitor performance in N–C materials. The core concept is that the functionalities of such materials are strongly influenced by the fraction, distribution and chemical configuration of nitrogen in the carbon network. The investigation is carried out on graphitic carbon nitride (g-CN), from which nitrogen is gradually removed to produce N–C materials having N/C ratios between 0.52 and 0.10. Materials with an N/C of 0.15 exhibit the highest capacitance, achieving 79.25 ± 3.8 F g^{-1} (volumetric capacitance of 1585 F cm^{-3}) at a current density of 1 A g^{-1}. These findings are particularly relevant to g-CN-derived disordered and non-graphitizing carbon systems but are also applicable to other forms of carbon. Precisely tuning the nitrogen content can guide targeted material synthesis and enable first-principles evaluation of an N–C material's suitability for supercapacitor applications.

Introduction

The functionalities of carbon materials in energy applications can be enhanced significantly by incorporating a heteroatom such as nitrogen (N) into the carbon network.[1–3] For crystalline carbons such as diamond and graphite, N can be incorporated in a controlled manner, and its lone electron pair can be precisely used for well-defined applications such as magnetic field sensing.[4,5] The same does not hold true for disordered carbons. The fraction, position, distribution and even characterization of N atoms in disordered carbon are difficult to achieve accurately.[6,7] This is primarily because such carbon materials are often complex non-graphitizing systems, which feature variable extents of graphitic content.[8] Small graphitic crystallites having turbostratic carbon layers, typically with five- and seven-membered rings are distributed within such materials, along with 5–7% fullerenes incorporated in them.[9] Consequently, while many examples of the use of non-graphitizing carbons containing N in both battery and supercapacitor devices have been reported,[10–12] and different morphologies,[13] pore sizes,[14,15] naturally abundant precursors,[15,16] and composites[17,18] have been explored, the exact mechanism and the influence of the fraction of N for energy storage systems of N-containing carbons remain largely unexplored.

The fraction of nitrogen in N–C materials is known to be strongly intertwined with their crystallinity.[8] The highest ratio of N to C that would yield a stable compound is 4/3, which is the case in stoichiometrically balanced graphitic carbon nitride (g-C_3N_4).[19,20] The lowest N-content is zero, that of pure carbon. Between these two extremes, an entire range of disordered N–C materials exist. They are the ones of interest in energy applications, as the presence of N in the carbon network locally changes the polarity of the carbon molecules (rings or sheets).[21,22] These slightly polarized regions serve as active sites that improve electron transfer reactions with the electrolyte. However, simply increasing the N fraction does not always lead to an improved electrochemical performance, as there is a trade-off between electrical conductivity and the number of polarized active sites in the material. In addition to the N/C ratio, these two properties depend upon the structural configuration(s) adopted by the N atoms in the carbon network, *i.e.*, whether N is present as pyrrolic, pyridinic and graphitic forms.[23–25] In various studies it has been suggested that pyridine N has the highest impact on the pseudocapacitive energy storage mechanism exhibited by the presence of N in a carbon system.[21,26,27]

N-containing carbon systems are commonly achieved *via* three pathways, (i) *in situ* incorporation during the synthesis of the carbon material, (ii) *ex situ* incorporation, *i.e.*, after the synthesis of the carbon material, and (iii) thermal de-nitrogenation of g-CN.[28,29] The first two methods yield N-containing carbons with a low N/C ratio (N/C ≤ 0.10) and offer less control of the configuration of N in the material. These materials generally contain pyrrolic, pyridinic and graphitic

School of Mechanical and Materials Engineering, Indian Institute of Technology Mandi, Kamand, HP, 175075, India. E-mail: swati@iitmandi.ac.in

† Equally contributing authors.

nitrogen species along with surface functional groups such as amines and amides.[30] The supercapacitor performance of such N–C systems with low N/C ratios has been widely investigated.[31–33] It is suggested that N–C materials with a high proportion of pyridinic and pyrrolic nitrogen species contribute significantly to pseudocapacitance (a combination of reversible faradaic reactions with electrical double layer type capacitance).[34] The third pathway involving the thermal denitrogenation of g-CN offers greater control over the nitrogen configuration in the resulting N–C materials. This method typically produces materials rich in pyridinic and graphitic nitrogen, with N/C ratios ranging from that of the g-CN precursor (1.33–0.35) down to as low as 0.01, depending upon the temperatures used in the process ≥2500 °C. In all aforementioned cases, individual N–C materials have been evaluated for their supercapacitor performance, without establishing any correlation with their N/C ratio, which is indeed the key player in their electrochemical activity. By and large, the following questions remain unanswered: (i) how the ratio of N/C in such materials influences the supercapacitor performance, (ii) what is the exact storage mechanism of such supercapacitors, and whether it is the same in all N–C materials, and finally, (iii) what is the optimum N/C ratio for device fabrication.

To study the effect of the N-content on supercapacitor performance of N–C materials featuring $0.10 \leq N/C \leq 1$, we prepared four different N–C materials exhibiting different N/C ratios by the following steps: (i) autoclave-assisted solvent-free heat-treatment of urea and citric acid to generate a g-CN material with a N/C ratio of 0.52, which is the first N–C material under investigation, (ii) further heat-treatment of this g-CN in a tube furnace at different target temperatures to methodically eliminate nitrogen and derive three materials with N/C ratios of 0.32, 0.15 and 0.10, respectively, and (iii) electrode preparation using these four materials for supercapacitor studies. These four N/C samples were characterized for their supercapacitor performance *via* cyclic voltammetry (CV), galvanostatic charge–discharge (GCD) tests, electrochemical impedance spectroscopy (EIS) and long term stability tests for 2500 GCD cycles.

Materials and methods

Materials

Urea (>99%) and citric acid (>99%) were procured from Qualigens, India and Sigma-Aldrich, USA, respectively. A Centrifuge: 5810 R (Eppendorf, India), Lindberg Blue M furnace (Thermo Scientific, TF55035C-1, USA) and planetary ball mill (Retsch PM-100, Germany) were used for centrifugation, heat-treatment, and ball milling processes, respectively.

Methods

Citric acid and urea, in a molar ratio of 1 : 6, were placed in a Teflon-lined autoclave (commonly referred to as a hydrothermal reactor) and heated at 200 °C for 1 hour. After cooling, the resulting mixture was dissolved in ethanol and subjected to sonication for 6 hours. This was followed by centrifugation at 2500 rpm for 10 minutes. The supernatant was used for a different study, and the solid residue was collected for further processing. The residue was thoroughly washed multiple times with ethanol and then air-dried at 80 °C for 6 hours to obtain the bulk graphitic carbon nitride (g-CN) material, denoted as N–C_2 (where 2 denotes its preparation temperature/100) and featuring a N/C ratio of 0.52.

N–C_2 was subsequently subjected to thermal treatment in a Lindberg Blue furnace. The sample was heated from room temperature to 600 °C at a ramp rate of 10 °C min^{-1}, with a dwell time of 1 hour, under a continuous nitrogen flow of 200 SCCM to ensure an inert atmosphere. The material obtained after this process was labeled as N–C_6 with an N/C ratio of 0.32. Similarly, heat treatments were conducted at 900 °C and 1300 °C under identical conditions to yield materials labelled as N–C_9 and N–C_{13} with an N/C ratio of 0.15 and 0.10 respectively, where the numeric designation corresponds to the hundredth digit of the treatment temperature.

Each material, N–C_2, N–C_6, N–C_9 and N–C_{13} was transferred into a 50 mL tungsten carbide jar containing ten 10 mm tungsten carbide balls. Wet ball milling was performed at 300 rpm for 3 hours (using 50 minutes milling followed by 10 minutes rest cycles). The weight ratio of milling balls to the N–C material to ethanol was maintained at 20 : 2 : 1. The resulting ball-milled N–C materials were subsequently used in electrode fabrication for electrochemical studies.

Material characterization

X-ray diffraction (XRD) of the N–C powder materials was performed on a SmartLab 9kW rotating anode X-ray diffractometer (Rigaku Corporation) having a monochromatic Cu Kα radiation (1.54 Å) source. The samples were scanned over the range of 2θ, 5°–90°, with a scan rate of 3° min^{-1}. The diffraction pattern was analyzed by Rietveld refinement using X'Pert HighScore Plus software. The values of interlayer spacing (d) were calculated using Bragg's diffraction law. Raman spectra of the N–C materials were recorded on a HORIBA LabRAM Jobin Yvon spectrometer with a 20 mW air-cooled argon laser (532 nm) for excitation. The spectra were recorded in the 300 to 3500 cm^{-1} spectral range using an ultralow frequency filter, 1800 grooves per mm grating, and Peltier cooled CCD for 150 s acquisition time. X-Ray photoelectron spectroscopy (XPS) spectra of the N–C materials were recorded on a Nexsa base (Thermo Fisher Scientific) surface analysis system with a micro-focused (400 μm, 72 W, 12 000 V) monochromatic Al-Kα source ($h\nu$ = 1486.6 eV, wavelength = 0.83 nm). The XPS survey scan spectra were recorded from 0 to 1350 eV binding energy. Data were collected at a pass energy of 40 eV with a step size of 0.1 eV. The narrow scan spectra of all the components were deconvoluted using XPS Peak41 curve-fitting software and Gaussian fit was used for peak fitting. A modified Shirley background, which includes additional constraints to ensure that the background intensity remains lower than the actual data at any point within the region, was employed for deconvolution. Adventitious carbon at 284.8 eV was used as the reference point. The nitrogen gas adsorption–desorption isotherms at 77 K for the N–C

powder materials were recorded on a Quantachrome Autosorb-iQ-MP/XR137 system to assess the Brunauer–Emmett–Teller (BET) surface area. Contact angle measurements of the pelletized N–C materials were done on an SEO Phoenix 300 Touch Contact Angle analyzer at room temperature and DI water droplets (15 μL volume) were used for measuring the contact angle. The electrical characterization of the pelletized N–C materials was performed using a KEITHLEY 4200 SCS system connected to a cascade probe station equipped with ~20 μm Ti probes. The voltage measurements were conducted using the four-point probe method, with a current range of −10 μA to 10 μA. The sheet resistance was calculated from the *I–V* data using the van der Pauw method. Elemental analysis of N–C powder materials was carried out using a B100003212 UNIQUBE system for simultaneous CHNS analysis, with the capability for oxygen determination *via* a thermal conductivity detector (TCD).

Electrochemical measurements

All the electrochemical measurements were performed in 1 M Na_2SO_4 electrolyte solution using a Biologic EC lab (SP-300) instrument. A platinum (Pt) wire and Ag/AgCl were employed as the counter and reference electrodes, respectively. At first, the ball milled N–C material, carbon black and polyvinylidene fluoride (PVDF) were mixed in a ratio of 8 : 1 : 1 with *N*-methyl-2-pyrrolidone (NMP) solvent. The prepared slurry was then coated on a carbon cloth (area: 1 × 1 cm^2; thickness: 0.5 mm) using a doctor blade, with the mass of the active material as 10 mg cm^{-2}. The coated sheet was dried at 80 °C for 12 h in a hot air oven and used as the working electrode. Electrochemical impedance spectroscopy (EIS) measurements were performed in the frequency range of 1 MHz to 0.1 Hz at 500 mV to investigate the resistive and capacitive behaviour of the N–C samples.

Results and discussion

The results of the microstructure analysis of all four N–C materials evaluated *via* XRD and Raman spectroscopy are provided in Fig. 1a and b respectively. A summary of the characterization of these N–C materials is provided in Table 1. The XRD peaks were fitted using JCPDS-87-1526 (hexagonal g-CN) for N/C = 0.52; both JCPDS-87-1526 and JCPDS-41-1487 (hexagonal graphite) for N/C = 0.32; and JCPDS-41-1487 alone for N/C = 0.15 and 0.10. The X-ray diffractograms (refer to Fig. 3a) of the N–C material with an N/C ratio of 0.52 reveals the presence of crystalline graphitic carbon nitride (g-CN) phases, as indicated by diffraction peaks at 12°, 27.2°, 34.8° and 48.9° corresponding to the (100), (002), (300), and (004) planes of g-CN, respectively. These findings are consistent with previous reports.[8] For the sample with an N/C ratio of 0.32, diffraction peaks from both g-CN and graphitic carbon phases are observed. The peak at 12° is attributed to the (100) plane of g-CN, while peaks at 24.8° and 43.2° correspond to the (002) and (100) planes of graphitic carbon, respectively. In the materials with N/C ratios of 0.15 and 0.10, the diffraction peaks at 24.9° and 43.4° arising from the (002) and (100) planes, confirm the presence of graphitic but disordered carbon phases. Interlayer spacing values for these N–C materials are listed in Table 1. Raman spectra (refer to Fig. 3b) of the N–C samples show features characteristic of disordered carbon, with distinct D, G and 2D bands observed at 1340, 1578, and 2780 cm^{-1}, respectively. Furthermore, the presence of a peak at 810 cm^{-1}, corresponding to the C–N stretching mode, in the spectra of materials with N/C ratios of 0.52, 0.32, and 0.15, confirms the incorporation of nitrogen into the structure. These results are in agreement with previous studies on similar materials.[35,36] The I_D/I_G ratio and the coherence length (L_a, nm),[37–39] calculated using the formula given in eqn (1), where λ is the laser wavelength of 532 nm, are the two indices that reveal the crystallinity in the (10) plane of the N–C materials. The values of these two indices are provided in Table 1, which confirm that the crystallinity in the (10) plane decrease initially and then further increases with a decreasing N/C ratio.

$$L_a = (2.4 \times 10^{-10}) \times (\lambda^4) \times \frac{I_G}{I_D} \quad (1)$$

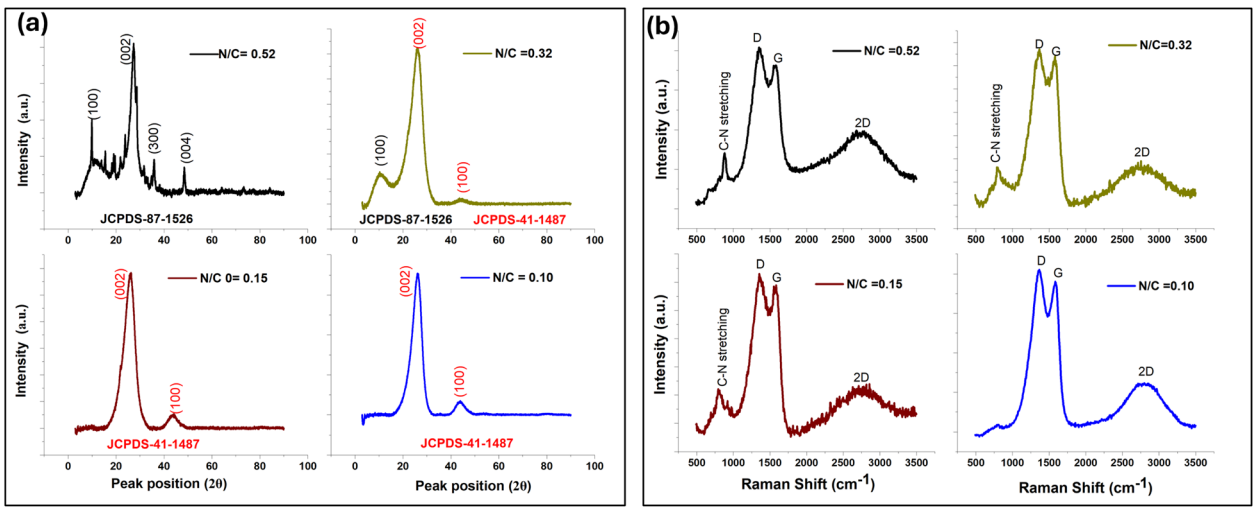

Fig. 1 (a) XRD plots and (b) Raman spectra of N–C materials with N/C ratios of 0.52, 0.32, 0.15 and 0.10.

Table 1 Results from the characterization of N–C materials featuring different N/C ratios

Sample code	N/C (atomic ratio)	d_{002} (nm)	I_D/I_G	L_a (nm)	σ ($\times 10^{-6}$ S cm^{-1})	XPS (atomic%)	CHNS[8] (weight%)	Contact angle (°)
N–C_2	0.52	0.328 ± 0.002	1.12 ± 0.01	17.10 ± 1.5	3 ± 1	C (57.74), N (17.77), O (24.49)	C (37), N (24.6), H (3.78), O (36.16)	33 ± 1
N–C_6	0.32	0.349 ± 0.002	1.19 ± 0.05	16.14 ± 1.5	12 ± 3	C (75.30), N (16.99), O (9.81)	C (61.53), N (25.95), H (2.93), O (12.58)	38 ± 1
N–C_9	0.15	0.342 ± 0.005	1.10 ± 0.02	17.30 ± 1.3	685 ± 26	C (86.88), N (10.76), O (2.47)	C (79.85), N (13.99), H (1.74), O (4.91)	56 ± 1
N–C_{13}	0.10	0.338 ± 0.004	1.01 ± 0.04	19.03 ± 1.7	1099 ± 49	C (95.01), N (3.78), O (1.31)	C (85.5), N (10), H (1), O (3.5)	81 ± 2

TEM images and the SAED pattern of the N–C material at N/C = 0.52 (see Fig. 2a and b), reveal a disordered g-CN material with percolated crystalline regions. At N/C = 0.32, the N–C material is converted into a turbostratic graphitic material with a high degree of disorder (see Fig. 2c and d). At N/C = 0.15, the disorder in the N–C material reduces as evident from the more graphitic regions in the TEM image and prominent rings in the SAED pattern (see Fig. 2e and f) and with a further decrease in the N/C ratio, at N/C = 0.10, more graphitic regions and prominent diffraction rings in the SAED patterns are observed in the HRTEM image (Fig. 2g) and SAED patterns (Fig. 2h) respectively. Detailed microstructure analysis of the N–C materials by TEM imaging is provided in an earlier publication.[8]

Surface elemental composition and functional groups of N–C materials confirmed by XPS are provided in Fig. 3a–d. The XPS survey spectrum is available in the SI (Fig. S1). Based on the C_{1s} spectra, the fitted peaks for the material with N/C = 0.52 (Fig. 3c) correspond to C=C (285.0 ± 0.2 eV), C–N/C–O (285.9 ± 0.2 eV), N=C–N (288.3 ± 0.1 eV), and O=C–O (288.8 ± 0.2 eV). For the material with N/C = 0.32 (Fig. 3b), 0.15 (Fig. 3c), and 0.10 (Fig. 3d), the C_{1s} peak fits indicate the presence of C=C, C–N/C–O, and O=C–O species.

The results from the N_2 adsorption studies indicate that the material with N/C = 0.15 exhibits the largest BET surface area among the four materials and the smallest average pore size (see Table 2 and Fig. S3 in the SI). This could be attributed to the fact that at this N/C ratio (T = 900 °C), the N–C material fully transitions from g-CN (N/C = 0.52) to a graphitic material with pyridine and graphitic N in it.[8] The smaller crystallite size and the presence of pyridine N in higher concentration are responsible for its higher surface area and lower pore size distribution compared to N/C = 0.10 (T = 1300 °C).

The different nitrogen species present on the material surfaces provide structural insights at specific N/C ratios. The three types of nitrogen species, identified from their N_{1s} spectral fit, are N–(C)3 (400.3 ± 0.1 eV), pyridinic N (398.6 ± 0.2 eV), and graphitic N (401.2 ± 0.2 eV). For N/C = 0.52, the fitted peaks include N–(C)3 species, representing N atoms bridging two triazine/hexagonal rings; pyridinic N, where N atoms alternate with C atoms in hexagons; and C–N species, attributed to

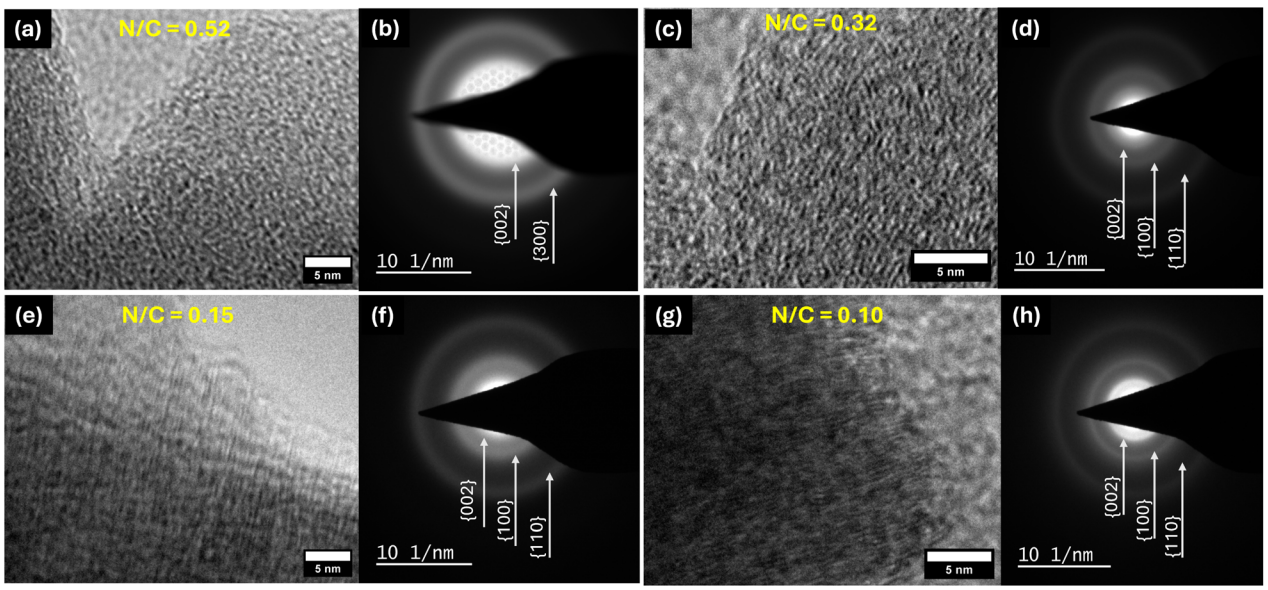

Fig. 2 (a, c, e and g) HRTEM micrographs and (b, d, f and h) SAED patterns of N–C materials with N/C ratios of 0.52, 0.32, 0.15 and 0.10 respectively.

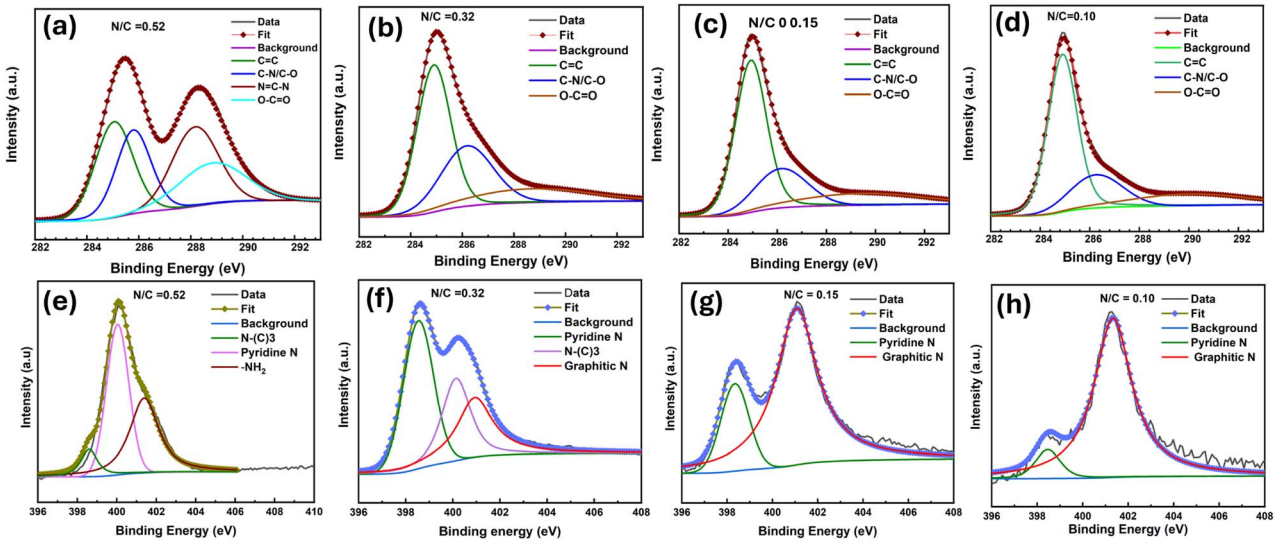

Fig. 3 (a–d) C_{1s} spectral fit and (e–h) N_{1s} spectral fit of N–C materials with N/C ratios of 0.52, 0.32, 0.15 and 0.10.

surface amine groups (see Fig. 3e). At N/C = 0.32 (see Fig. 3f), pyridinic N, N–(C)3, and graphitic N species are observed. For N/C = 0.15 (see Fig. 3g) and N/C = 0.10 (see Fig. 3h), only pyridinic N and graphitic N species are identified from the peak fits. The proportions of these nitrogen species are detailed in the SI (Fig. S2), from which the ratio of pyridinic N to graphitic N is calculated.

A comparison of the cyclic voltammograms of the N–C materials within a voltage window of 0 to 1 V is depicted in Fig. 4a. As shown, the CVs of N–C_2 (N/C = 0.52), N–C_6 (N/C = 0.32), N–C_9 (N/C = 0.15) and N–C_{13} (N/C = 0.10) at a scan rate of 10 mV s^{-1} exhibit a quasi-rectangular shape, indicating pseudocapacitive behavior of all the materials.[34] The specific capacitance (C_{sp}) calculated from the cyclic voltammograms (Fig. 4a) using eqn (2) is 69, 78, 81 and 34 F g^{-1} for N–C_2, N–C_6, N–C_9 and N–C_{13} respectively. The area under the CV curves is the highest for N–C_9 at an N/C ratio of 0.15, indicating its high electrochemically active surface area, and hence high capacitance.

Nitrogen incorporation into the carbon network enhances electron donor properties, improving electron transfer kinetics at the electrode/electrolyte interface, enabling reversible redox reactions, and thereby contributing to pseudocapacitance in otherwise EDLC-type carbon-based materials.[28] The extent of pseudocapacitance is also influenced by the chemical nature and type of bonding of nitrogen in the N–C systems, such as whether it is part of a compound (like g-CN) or present as defects in carbon. The quasi-rectangular shape of the cyclic voltammograms becomes more pronounced with decreasing nitrogen content, as the N/C ratio reduces from 0.52 (for N–C_2) to 0.15 (N–C_9). Notably, it is N–C_9 (N/C ratio 0.15), and not N–C_{13} (N/C = 0.10) that displays the most pronounced quasi-rectangular CV profile, signaling a reverse transition from pseudocapacitive to EDLC behavior as the N/C ratio further decreases.

Interestingly, we found that an increase in N content does not directly correlate with a higher capacitance. The capacitive performance of N–C systems is also strongly influenced by their electrical conductivity and nitrogen configuration. For crystalline g-CN with an N/C ratio of 1.33, N is present alternatively with carbon on hexagonal rings and therefore the electron density is balanced. Here, nitrogen does not contribute to reversible redox reactions, which are essential for pseudocapacitance. Therefore, the supercapacitors made of pure g-CN are essentially of EDLC type.[40] However, in nitrogen-deficient g-CN systems (such as N–C_2, N/C = 0.52), the electron density is more shifted towards N atoms, and N atoms actively participate in redox reactions promoting pseudocapacitance.[12] In carbon systems with N atoms present as defects (as in the case of N–C_6, N–C_9, and N–C_{13}), the N atoms more actively participate in reversible-redox reactions due to a polarity shift between N and C atoms. These polarised atoms in a carbon material facilitate electrolyte ion diffusion and adsorption, promoting pseudocapacitance.[41] Additionally, the conductive carbon network

Table 2 Results from the adsorption studies of N–C materials featuring different N/C ratios

Sample code	N/C (atomic ratio)	BET surface area (m^2 g^{-1})	Pore volume (m^3 g^{-1})	Average pore diameter (nm)
N–C_2	0.52	19.82 ± 1	0.12 ± 0.03	30.11 ± 1.3
N–C_6	0.32	95.53 ± 3	0.35 ± 0.05	21.33 ± 1
N–C_9	0.15	132.07 ± 6	0.42 ± 0.02	8.50 ± 0.5
N–C_{13}	0.10	21.05 ± 1.5	0.11 ± 0.01	22.62 ± 0.9

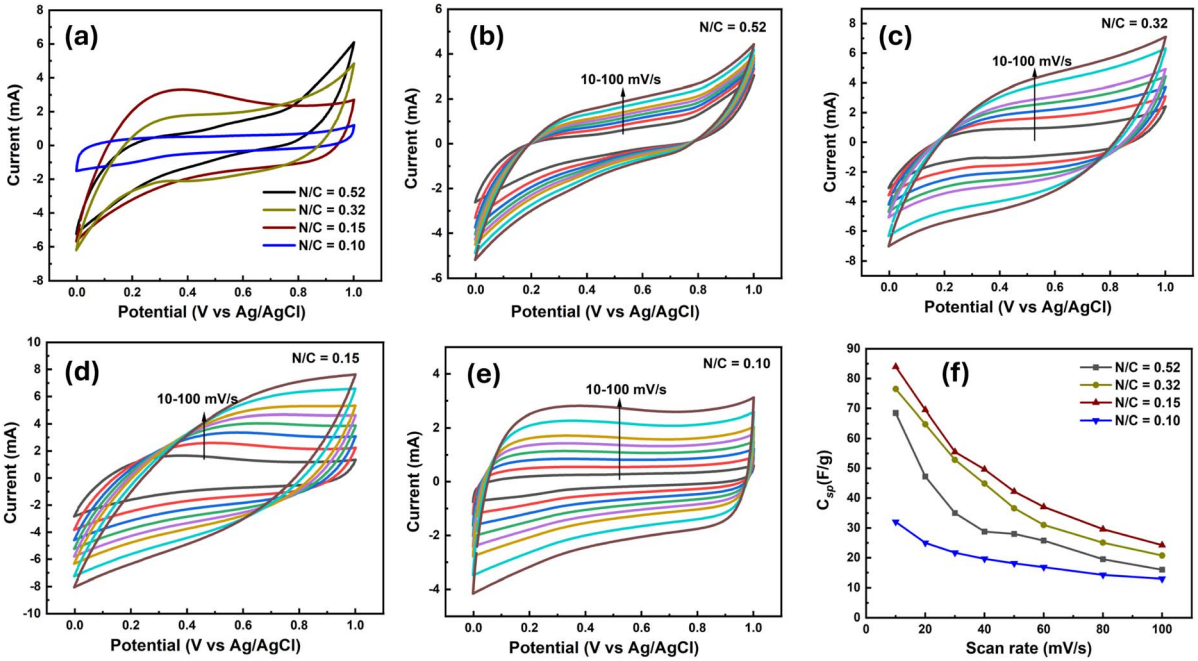

Fig. 4 (a) Comparative cyclic voltammograms of N–C materials with N/C ratios of 0.52, 0.32, 0.15 and 0.10. Cyclic voltammograms at different scan rates for N–C materials with N/C ratios of (b) 0.52, (c) 0.32, (d) 0.15, and (e) 0.10. (f) Specific capacitance *vs.* scan rate plot for N–C materials with N/C ratios of 0.52, 0.32, 0.15 and 0.10.

reduces resistance at the electrode/electrolyte interface, thereby enhancing the overall capacitance.[25]

The capacitance of N-containing carbon also depends on the configuration of N, such as pyrrolic N, pyridine N or graphitic N present in the material.[42] The area under the cyclic voltammograms is highest for N–C_9 (N/C = 0.15), which benefits from a balance between surface area, electrical conductivity, wettability, and pyridine N content, all key characteristics of effective energy storage materials.[43] The reverse transition of the capacitive behavior from pseudo to EDLC for N–C_{13} can be attributed to a lower fraction of pyridine N species[44,45] (see Fig. S1). CV measurements at different scan rates for the N–C systems are shown in Fig. 4b–e. The C_{sp} calculated from these cyclic voltammograms using eqn (2) at different scan rates is provided in Fig. 4f. Even at higher scan rates, the cyclic voltammograms remain consistent for all N–C systems, with an increase in current response, likely due to an increase in areal capacitance.

To quantify the fraction of EDLC and faradaic reactions to the overall specific capacitance of each N–C material, the Trasatti methodology was employed.[42] An initial scan was carried out at rates ranging from 10 mV s^{-1} to 100 mV s^{-1} to obtain the cyclic voltammograms (CVs) of each specimen. Following this data acquisition phase, the corresponding gravimetric specific capacitance (C_{sp}) was calculated using the formula presented in eqn (2). In this expression, A denotes the area enclosed by the CV curve, while m, v, and δV represent the mass of the material in grams, the scan rate in mV s^{-1}, and the potential window in volts, respectively. The gravimetric capacitances, expressed as $C_{sp}{}^{-1}$, were plotted against the square root of the scan rates, denoted as $v^{0.5}$. This was performed with the expectation that a linear relationship between these variables would be revealed, under the assumption of semi-infinite ion diffusion. The observed correlations can be described using eqn (3) and (4).

$$C_{sp} = \frac{A}{2mv\delta v} \quad (2)$$

$$C_{sp}{}^{-1} = kv^{0.5} + C_T{}^{-1} \quad (3)$$

$$C_{sp} = kv^{-0.5} + C_{EDLC} \quad (4)$$

Here C_{sp} refers to the experimentally determined gravimetric capacitance, v corresponds to the scan rate, and C_T and C_{EDLC} represent the total capacitance and the electrical double-layer capacitance, respectively. By performing a linear fit on the plot and extrapolating the line to the y-axis, the maximum value of the EDLC is determined. The maximum capacitance from faradaic reactions is then obtained by subtracting the value of C_{EDLC} from the total capacitance C_T. The results derived through this method are presented in Table 3. It is found that the material with an N/C ratio of 0.15 exhibits the highest value of capacitance contribution from faradaic reactions. Additionally, the rate capability index (b) is critical for understanding the charge storage mechanism in supercapacitors. The b values for the N–C materials are provided in Table 3 and the values lie between 0.5 and 1. This indicate a hybrid charge storage mechanism indicative of pseudocapacitive materials, with N/C = 0.10 exhibiting the highest rate capability among the four materials.

To further study the effect of the N/C ratio on the supercapacitor performance of the N–C systems, GCD measurements

Table 3 Contributions of EDLC capacitance and faradaic capacitance to the overall capacitance of N–C materials. In the sample codes, the subscripted number denotes the preparation temperature/100

Sample code	N/C (atomic ratio)	EDLC ($F\ g^{-1}$)	Faradaic capacitance ($F\ g^{-1}$)	% EDLC	% faradaic capacitance	Rate performance index, b
N–C_2	0.52	20.90	42.75	32.84	67.16	0.6833
N–C_6	0.32	24.40	52.15	31.97	68.03	0.6696
N–C_9	0.15	25.99	59.15	30.52	69.47	0.7284
N–C_{13}	0.10	17.15	12.30	58.62	41.38	0.8412

were conducted at various current densities, as depicted in Fig. 5a–f. Fig. 4a illustrates the comparative GCD curves of the four N–C materials at a current density of 1 A g^{-1}. The GCD curves exhibited a nearly triangular shape (Fig. 4a), with a non-linear discharge pattern characteristic of pseudocapacitive behavior. This observed charge–discharge pattern aligns with the behavior seen in cyclic voltammograms, further confirming the pseudocapacitive nature. C_{sp} values for the N–C materials at a current density of 1 A g^{-1} calculated using the formula provided in eqn (5) are 64.67 ± 2.5, 71.29 ± 3.2, 79.25 ± 3.8 and 25.55 ± 1.9 F g^{-1} for N/C = 0.52, N/C = 0.32, N/C = 0.15 and N/C = 0.10 respectively. The GCD curves at different current densities for the N–C systems are presented in Fig. 4b–e, revealing that the non-linear discharge patterns are maintained even at higher current densities. The plot of C_{sp} derived from these GCD curves (Fig. 5b–e) at different current densities is provided in Fig. 5f. The corresponding areal and volumetric capacitance values corresponding to the gravimetric capacitances at different current densities are provided in Table S1 of the SI.

$$C_{sp} = \frac{I\delta t}{m\delta V} \quad (5)$$

where I is the current applied, δt is the discharge time, m is the mass loading, and δV represents the potential window.

The Nyquist plots of N/C = 0.52 (Fig. 6a and c) (also see the enlarged Nyquist plot in Fig. 6b) exhibit a linear trend without a noticeable semicircle region, indicating a low charge transfer resistance (R_{ct}) at the electrode/electrolyte interface for the N–C material. The R_{ct} values can be correlated with the porous nature of these materials, indicating that N/C = 0.52 has a lower fraction of meso and micro pores. The presence of a semicircle in the high-frequency region in the Nyquist plots of N/C = 0.32, N/C = 0.15, and N/C = 0.10 (see Fig. 6b, and also see Fig. 6d–f) indicates the presence of smaller sized pores, indicating their high surface area. The R_{ct} values are 75.9, 12.8 and 5.9 Ω respectively for N/C = 0.32, N/C = 0.15, and N/C = 0.10 respectively. The equivalent series resistance (ESR) values were calculated to be 23.58, 1.52, 1.59, and 1.06 Ω for N/C = 0.52, N/C = 0.32, N/C = 0.15, and N/C = 0.10 respectively. In the high

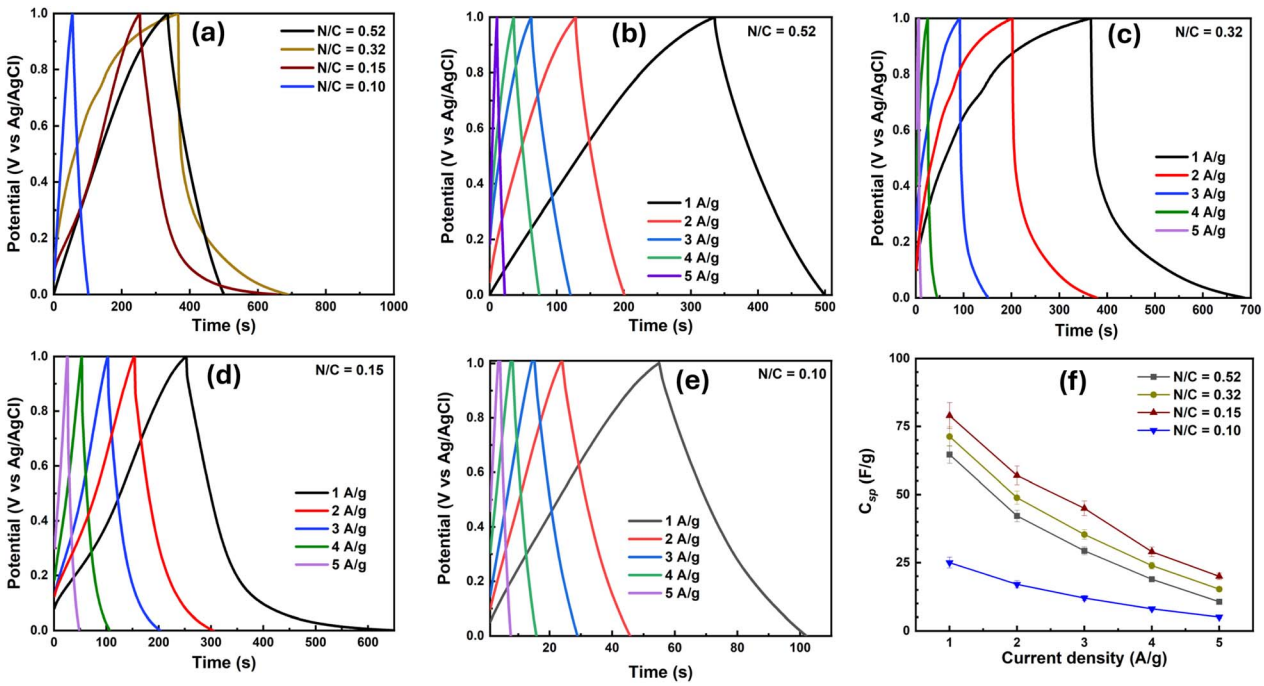

Fig. 5 (a) Comparative galvanostatic charge–discharge curves of N–C materials with N/C ratios of 0.52, 0.32, 0.15 and 0.10 at 1 A g^{-1}. Galvanostatic charge–discharge curves at different current densities for N–C materials with N/C ratios of (b) 0.52, (c) 0.32, (d) 0.15, and (e) 0.10. (f) Specific capacitance *vs.* current density plot for N–C materials with N/C ratios of 0.52, 0.32, 0.15 and 0.10.

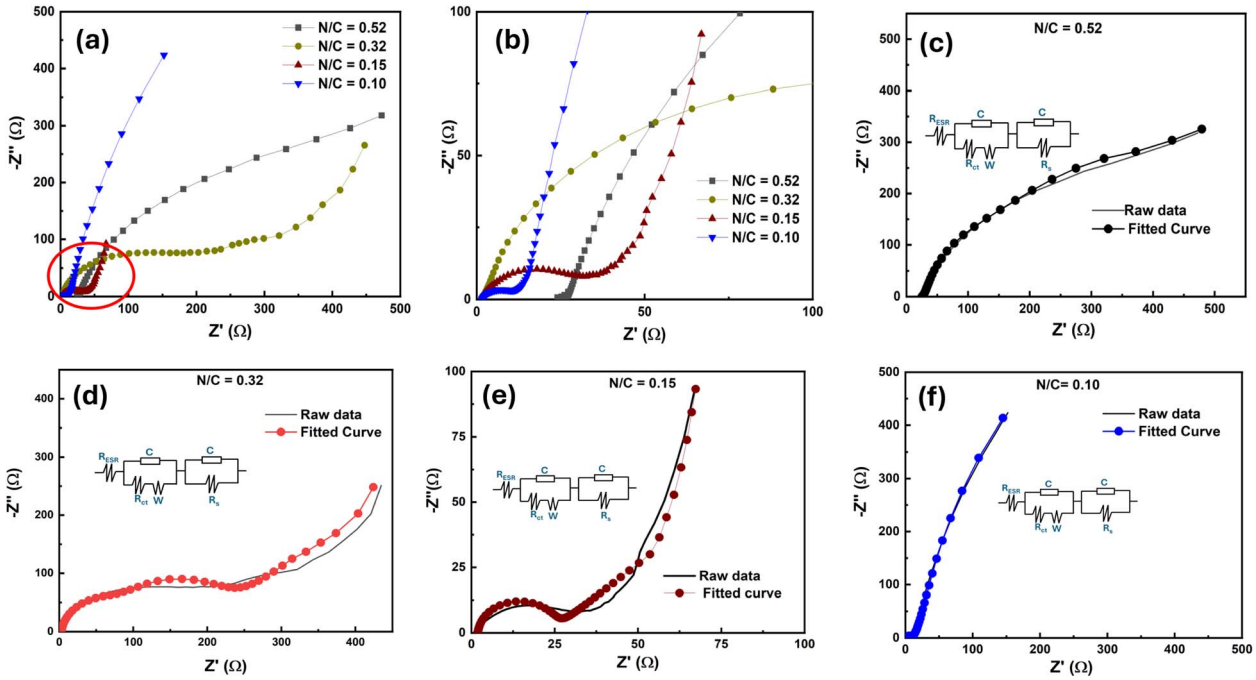

Fig. 6 (a) Comparative Nyquist plots and (b) enlarged Nyquist plot of the red encircled region in (a), obtained from electrochemical impedance spectroscopy for N–C materials with N/C ratios of 0.52, 0.32, 0.15 and 0.10. (c–f) Fitted Nyquist plots with equivalent circuit diagrams for (c) N/C = 0.52, (d) N/C = 0.32, (e) N/C = 0.15 and (f) N/C = 0.10.

frequency region, the Nyquist plot of N–C_6 and N–C_9 resemble that of pseudocapacitive carbon materials while that of N/C = 0.10 resembles the Nyquist plot of EDLC-type carbon materials.[46] Evidently, N/C = 0.15 exhibits the overall lowest resistance, indicative of its high capacitance. Individual fitted Nyquist plots of the four N–C materials with their equivalent circuit diagrams are provided in Fig. 6c–f. Additionally, N/C = 0.52, 0.32 and 0.15 exhibited phase angles between −45° and 70° indicating pseudocapacitive behavior, and in the case of N/C = 0.10, phase angles at lower frequency indicated EDLC dominant behavior (see Fig. S4).

The long-term stability of the N–C materials was evaluated through GCD cycling for over 2500 cycles at a current density of 25 A g^{-1} (refer to Fig. 7a–d). For the sample with N/C = 0.52 (Fig. 7a), the capacitance retention increased to 102% around the 1000th cycle, after which it began to decline, reaching 94.30% at the end of 2500 cycles. The coulombic efficiency remained steady at 55.50%. In the case of N/C = 0.32 (Fig. 7b), the capacitance consistently increased with cycling, achieving a retention of 105.2% after 2500 GCD cycles, with the coulombic efficiency stably maintained at 67.10%. For N/C = 0.15 and 0.10 (Fig. 7c and d), capacitance retention remained constant (100%) up to 1500 cycles, followed by a gradual decline. Final capacitance retentions of 96.10% and 98.50% were observed for N/C = 0.15 and 0.10, respectively. At these lower N/C ratios, the N–C materials demonstrated high coulombic efficiencies of 98.90% at the end of 2500 cycles. A high coulombic efficiency of 99.98% is maintained even at low current density of 1 A g^{-1} for 10k cycles in the case of N/C = 0.15 (see Fig. S5).

The variation in long-term stability results of the N–C materials can be attributed to differences in the N/C ratios and the distinct configurations of nitrogen within the graphitic framework. For samples with N/C = 0.52 and 0.32, which possess a high pyridine content, the observed increase in capacitance after several hundred GCD cycles is due to electrochemical activation of the electrode.[47] With continued GCD cycling, the electrolyte penetrates deeper into the electrode, enabling access to active sites, particularly pyridine N, that contribute to pseudocapacitance, increasing the overall capacitance. However, this elevated pyridine N content,[48] along with increased oxygen levels, promotes parasitic side reactions such as the oxygen evolution reaction (OER) at the electrode/electrolyte interface of materials with N/C = 0.52 and 0.32, accounting for the lower coulombic efficiency. As the N/C ratio decreases, the coulombic efficiency improves due to the reduced presence of pyridine N, which in turn limits parasitic reactions like the OER. Furthermore, at lower N/C ratios (associated with higher heat-treatment temperatures), the oxygen content in the materials is also reduced (see XPS data in Table 1 and Fig. S1). Consequently, the lower coulombic efficiencies observed in high N/C ratio materials can be attributed to parasitic reactions involving both pyridine N and oxygen species.

As shown in Fig. 8a, the variation of C_{sp} calculated from the CV and GCD plots at 10 mV s^{-1} and 1 A g^{-1} for different N/C ratios is shown. The trend of capacitance is similar for the values calculated from CV and GCD, indicating that the N–C material at N/C = 0.15 exhibits the highest capacitance. All electrochemical data allude to the fact that the supercapacitive performance of N–C materials, in terms of their long time stability and coulombic efficiencies, peaks at an N/C ratio of around 0.15, particularly when the ratio of pyridine N (N6) to

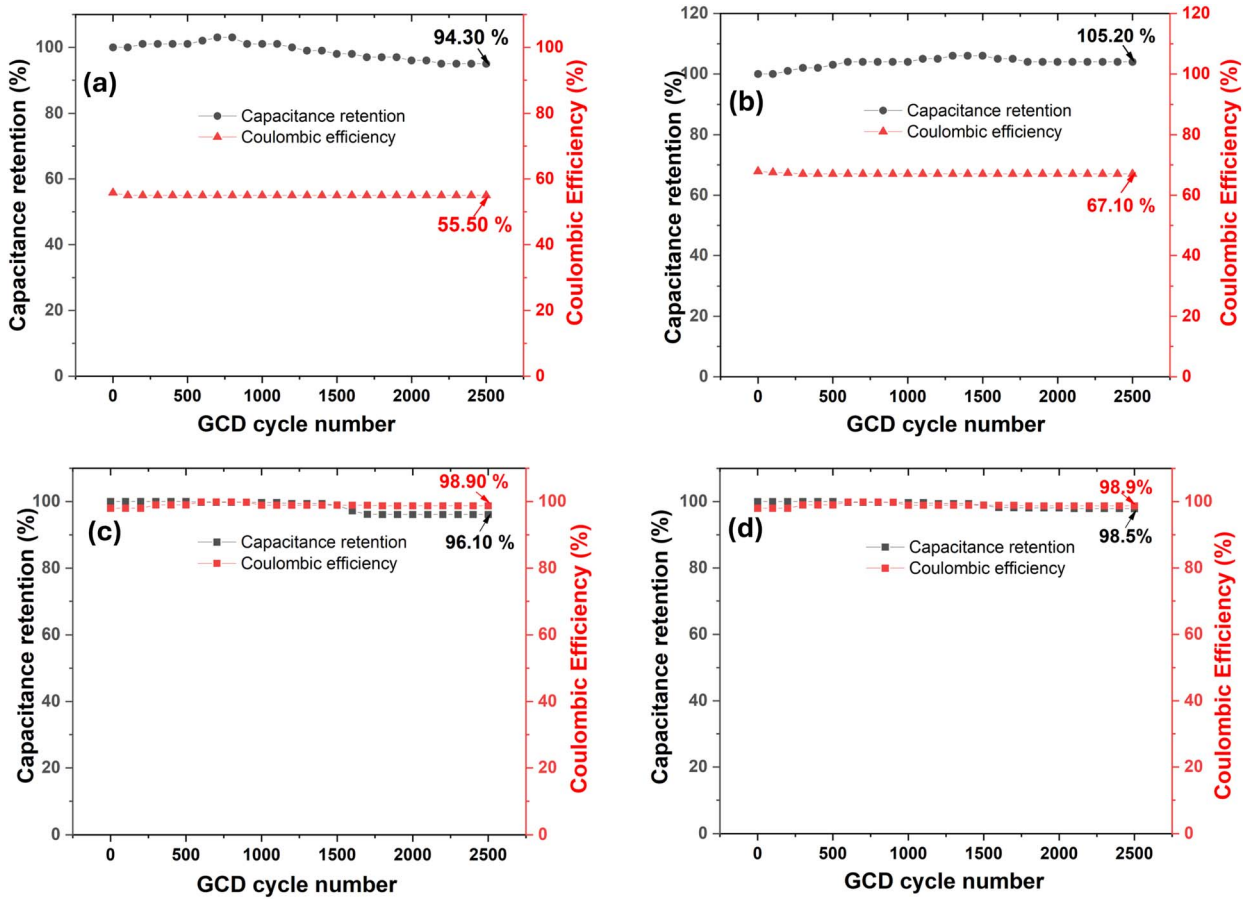

Fig. 7 Capacitance retention and coulombic efficiency plots measured *via* GCD for 2500 cycles for N–C materials (a) N/C = 0.52, (b) N/C = 0.32, (c) N/C = 0.15 and (d) N/C = 0.10.

graphitic N (NQ) is 0.33 (see Table 1). At this N6/NQ ratio, the N–C material exists as a disordered carbon where the sp^2 carbon sheets in the graphitic crystallites have N6 and NQ atoms present as defects. In such a disordered carbon, N6 provides active sites for reversible redox reactions and contributes to a high surface area, while NQ enhances electrical conductivity and limiting the parasitic side reactions. Both nitrogen species improve wetting characteristics in the otherwise hydrophobic carbon material. This combination creates an optimal balance between conductivity, wettability and surface area, leading to superior electrochemical performance (see Fig. 8b). Further decreasing the N/C ratio through higher-temperature heat treatment is expected to reduce the capacitance, with the resulting supercapacitor behavior dominated by EDLC. This treatment likely converts all pyridinic nitrogen into graphitic nitrogen, making the material more graphitic and eliminating active sites necessary for promoting pseudocapacitance.

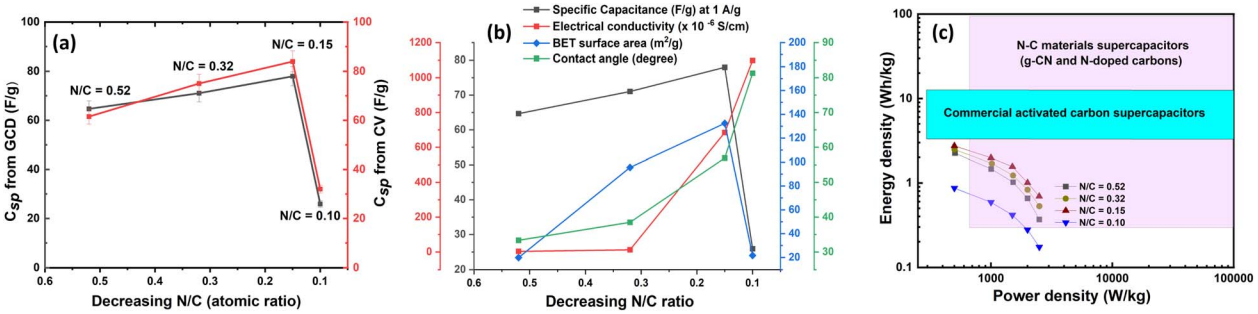

Fig. 8 (a) Relation of the N/C atomic ratio of the N–C materials with specific capacitance deduced from cyclic voltammetry at 10 mV s^{-1} and galvanostatic charge–discharge tests at 1 A g^{-1} from the three-electrode study, (b) relation of the N/C ratio with other material properties which influence the capacitance in N–C materials, and (c) comparative Ragone plot of the N–C materials.

In Fig. 8c, the Ragone plot of the N–C materials compared to reported N–C materials and commercial activated carbon devices is shown. Device level (symmetric supercapacitor) capacitance of the N–C materials was calculated from the three electrode capacitance using eqn (6) (data provided in SI, Fig. S6) from which the energy density, E (Wh kg^{-1}) and power density, P (W kg^{-1}) were calculated using eqn (7) and (8) respectively. In these equations, C is the capacitance, V is the voltage window and t is the discharge time in seconds. The N–C materials reported in this work fall in the range of supercapacitive N–C materials[12,28] in the Ragone plot and their E and P values are slightly lower than that of commercial activated carbon supercapacitors.[49] Further activation of the N–C materials by KOH treatment/CO_2 activation can enhance their device-level performance. Three-electrode supercapacitor study of the N–C material with N/C = 0.15 in 1M $TEABF_4$/AN (see Fig. S7 in the SI) confirms that the material is stable in organic electrolytes as well. This suggests that exploring the device-level supercapacitor performance of such N–C materials in various electrolyte systems could pave the way for their application in powering next-generation wearable electronic devices.

$$C_{sp}(\text{device}) = \frac{C_{sp}(\text{electrode})}{4} \quad (6)$$

$$E = \frac{1}{2} \times CV^2 \times \frac{1}{3.6} \quad (7)$$

$$P = \frac{E \times 3600}{t} \quad (8)$$

Conclusion

In conclusion, we investigated the effect of nitrogen content on the supercapacitor performance of N–C materials with N/C ratios ranging from 0.52 to 0.10. Such materials are typically prepared by thermal denitrogenation of g-CN, and are devoid of pyrrolic N. The presence of pyridinic N plays a key role in enhancing capacitance, with an optimal pyridinic to graphitic N ratio of 0.33. It was found that for this class of materials, an increase in the N/C ratio does not directly correlate with an increase in capacitance. Supercapacitor performance depends on the crystal structure at that particular N/C ratio. The N/C ratio determines whether the material exists as g-CN or as a carbon with N incorporated in defect sites. This structural disparity at varying N/C ratios impacts key physicochemical properties like surface area, conductivity and wettability, which in turn dictate the electrochemical behavior. The highest capacitance recorded was 79.25 ± 3.8 F g^{-1} at 1 A g^{-1} for the material with N/C = 0.15.

This work establishes a foundation for understanding the role of N/C ratios in N–C materials derived from g-CN precursors. Our findings can serve as useful guidelines for optimizing the N content or N/C ratio in electrode materials designed for high-performance supercapacitors. N–C materials are expected to provide a significant boost to the existing supercapacitor technology, facilitating cheaper and greener alternatives to elemental carbon. The results reported here enable researchers to evaluate the potential of their N–C material in energy applications simply by conducting elemental analysis and XPS. Future work can focus on studying the impact of O content and the variation in O species on supercapacitor performance.

Author contributions

M. D.: conceptualization, design, data analysis, and drafting of the manuscript, J. S.: data acquisition and drafting of the manuscript and S. S.: manuscript review & editing, funding acquisition, supervision.

Conflicts of interest

The authors declare that there are no conflict(s) of interest.

Data availability

Source data are available from the corresponding author (S. S.) upon reasonable request.

All data supporting the findings of this study are included in the paper and its supplementary information (SI). Supplementary information is available. See DOI: **https://doi.org/10.1039/d5ta06469d**.

Acknowledgements

M. D. and J. S. would like to thank the Ministry of Education, Government of India, for their doctoral fellowships. The authors acknowledge the Advanced Materials and Research Center and the Center for Design and Fabrication of Electronic Devices, IIT Mandi, for providing access to characterization facilities.

References

1 M. Inagaki, M. Toyoda, Y. Soneda and T. Morishita, Nitrogen-doped carbon materials, *Carbon*, 2018, **132**, 104–140.
2 H. Guo, T. Sun, Q. Yin, X. Li, Z. Chen and X. Ma, Heteroatom-doped lignin-derived carbon material: performance and application, *Sustainable Energy Fuels*, 2024, **8**, 1369–1388.
3 L. Liu, W. Zhang, B. Lu, Z. Cheng, H. Cao, J. Li, Z. Fan and X. An, Controllable heteroatoms doped electrodes engineered by biomass based carbon for advanced supercapacitors: A review, *Biomass Bioenergy*, 2024, **186**, 107265.
4 Y. Zheng, C. Li, J. Liu, J. Wei and H. Ye, Diamond with nitrogen: states, control, and applications, *Funct. Diam.*, 2021, **1**, 63–82.
5 H. Zhou, X. Zhang, X. Zhang, F. Yuan, X. Wang, S. Yan, J. Wang, C. Li and Z. Sun, N-doped microcrystalline graphite for boosting peroxymonosulfate activation with highly efficient degradation of bisphenol A, *Carbon*, 2024, **216**, 118579.

6 K. Mainali, S. H. Mood, M. R. Pelaez-Samaniego, V. Sierra-Jimenez and M. Garcia-Perez, Production and applications of N-doped carbons from bioresources: A review, *Catal. Today*, 2023, **423**, 114248.

7 I. Jeon, H. Noh and J. Baek, Nitrogen-Doped Carbon Nanomaterials: Synthesis, Characteristics and Applications, *Chem.–Asian J.*, 2020, **15**, 2282–2293.

8 M. Devi, P. Pandey and S. Sharma, Crystalline–disordered–crystalline transition in nitrogen–carbon materials, *J. Appl. Phys.*, 2025, **137**, 025104.

9 S. Sharma, S. Zorzi, V. Cristiglio, R. Schweins and C. Mondelli, Quantification of Buckminsterfullerene (C_{60}) in non-graphitizing carbon and a microstructural comparison of graphitizing and non-graphitizing carbon via Small Angle Neutron Scattering, *Carbon*, 2022, **189**, 362–368.

10 S. Kaushal and J. Andrews, A review on the nitrogenated carbon materials and their electrochemical performance for energy storage applications, *Int. J. Hydrogen Energy*, 2025, **100**, 1231–1245.

11 Q. Jiang, Y. Cai, X. Sang, Q. Zhang, J. Ma and X. Chen, Nitrogen-Doped Carbon Materials As Supercapacitor Electrodes: A Mini Review, *Energy Fuels*, 2024, **38**, 10542–10559.

12 M. Devi, S. Upadhyay, R. A. Mir, N. Kumar and S. Sharma, Synthetic waste derived graphitic carbon nitride (g-CN) and g-CN/carbon hybrid for supercapacitors, *J. Energy Storage*, 2023, **73**, 109067.

13 J. Zhao, H. Lai, Z. Lyu, Y. Jiang, K. Xie, X. Wang, Q. Wu, L. Yang, Z. Jin, Y. Ma, J. Liu and Z. Hu, Hydrophilic Hierarchical Nitrogen-Doped Carbon Nanocages for Ultrahigh Supercapacitive Performance, *Adv. Mater.*, 2015, **27**, 3541–3545.

14 A. Adeniji, A. Beda, P. Fioux and C. Matei Ghimbeu, Engineering nitrogen-doped porous carbon positive electrodes for high-performance sodium-ion capacitors: the critical role of porosity, structure and surface functionalities, *J. Mater. Chem. A*, 2025, **13**, 14896–14914.

15 M. Prieto, G. J. Ellis, V. Budarin, E. Morales, M. Naffakh and P. S. Shuttleworth, Understanding pore size relation in cellulose-derived, nitrogen-doped, hydrothermal carbons for improved supercapacitor performance, *J. Mater. Chem. A*, 2024, **12**, 29698–29707.

16 G. Zhu, L. Ma, H. Lv, Y. Hu, T. Chen, R. Chen, J. Liang, X. Wang, Y. Wang, C. Yan, Z. Tie, Z. Jin and J. Liu, Pine needle-derived microporous nitrogen-doped carbon frameworks exhibit high performances in electrocatalytic hydrogen evolution reaction and supercapacitors, *Nanoscale*, 2017, **9**, 1237–1243.

17 G. Zhu, T. Chen, L. Wang, L. Ma, Y. Hu, R. Chen, Y. Wang, C. Wang, W. Yan, Z. Tie, J. Liu and Z. Jin, High energy density hybrid lithium-ion capacitor enabled by Co_3ZnC@N-doped carbon nanopolyhedra anode and microporous carbon cathode, *Energy Storage Mater.*, 2018, **14**, 246–252.

18 J. Yesuraj, P. Naveenkumar, M. Maniyazagan, H.-W. Yang, S.-J. Kim and K. Kim, Fabrication of N-doped carbon coated $CoFeS_2$ anchored rGO nanosheet composites: a twin carbon design for Li-ion storage and high energy density supercapacitor applications, *J. Mater. Chem. A*, 2025, **13**, 21830–21846.

19 M. Inagaki, T. Tsumura, T. Kinumoto and M. Toyoda, Graphitic carbon nitrides ($g\text{-}C_3N_4$) with comparative discussion to carbon materials, *Carbon*, 2019, **141**, 580–607.

20 J. Miao, W. Geng, P. J. J. Alvarez and M. Long, 2D N-Doped Porous Carbon Derived from Polydopamine-Coated Graphitic Carbon Nitride for Efficient Nonradical Activation of Peroxymonosulfate, *Environ. Sci. Technol.*, 2020, **54**, 8473–8481.

21 H. Chen, F. Sun, J. Wang, W. Li, W. Qiao, L. Ling and D. Long, Nitrogen Doping Effects on the Physical and Chemical Properties of Mesoporous Carbons, *J. Phys. Chem. C*, 2013, **117**, 8318–8328.

22 J. D. Wiggins-Camacho and K. J. Stevenson, Effect of Nitrogen Concentration on Capacitance, Density of States, Electronic Conductivity, and Morphology of N-Doped Carbon Nanotube Electrodes, *J. Phys. Chem. C*, 2009, **113**, 19082–19090.

23 R. Ganesan and J. R. Xavier, Fabrication of polythiophene/graphitic carbon nitride/V_2O_5 nanocomposite for high-performance supercapacitor electrode, *Mater. Sci. Eng., B*, 2024, **300**, 117101.

24 Q. Chu, Z. Chen, C. Cui, Y. Zhang, X. Li, G. Liu, H. Yang, Y. Cui, Y. Li and Q. Liu, Pyrrolic-N/C = O cooperative assisted in hollow porous carbon with ultra-high electrochemical performance for Zn-ion hybrid supercapacitors, *Appl. Surf. Sci.*, 2024, **654**, 159461.

25 B.-H. Xiao, R.-T. Lin, K. Xiao and Z.-Q. Liu, A highly compressible, nitrogen doped carbon foam based all pseudo-capacitance asymmetric supercapacitors, *J. Power Sources*, 2022, **530**, 231307.

26 D. Hulicova-Jurcakova, M. Seredych, G. Q. Lu and T. J. Bandosz, Combined Effect of Nitrogen- and Oxygen-Containing Functional Groups of Microporous Activated Carbon on its Electrochemical Performance in Supercapacitors, *Adv. Funct. Mater.*, 2009, **19**, 438–447.

27 G. Lota, B. Grzyb, H. Machnikowska, J. Machnikowski and E. Frackowiak, Effect of nitrogen in carbon electrode on the supercapacitor performance, *Chem. Phys. Lett.*, 2005, **404**, 53–58.

28 Y. Deng, Y. Xie, K. Zou and X. Ji, Review on recent advances in nitrogen-doped carbons: preparations and applications in supercapacitors, *J. Mater. Chem. A*, 2016, **4**, 1144–1173.

29 Y. Gao, T. Li, Y. Zhu, Z. Chen, J. Liang, Q. Zeng, L. Lyu and C. Hu, Highly nitrogen-doped porous carbon transformed from graphitic carbon nitride for efficient metal-free catalysis, *J. Hazard. Mater.*, 2020, **393**, 121280.

30 K. Xiong, Z. Liu, L. Ren, D. Li, K. Dong, L. Yang and X. Zhang, N and O dual-doped porous carbon transformed from graphitic carbon nitride as a peroxymonosulfate activator for tetracycline hydrochloride degradation, *New J. Chem.*, 2025, **49**, 855–864.

31 B. Krüner, A. Schreiber, A. Tolosa, A. Quade, F. Badaczewski, T. Pfaff, B. M. Smarsly and V. Presser, Nitrogen-containing

novolac-derived carbon beads as electrode material for supercapacitors, *Carbon*, 2018, **132**, 220–231.

32 R. Jangra, P. Mahendia, M. Karakoti, N. Sahoo, A. Srivastava, O. Sinha, T. D. Clemons, U. Deshpande and S. Mahendia, $ZnCl_2$-assisted conversion of nitrogen-containing biomass carbon from marigold flower: Toward highly porous activated nitrogen-doped carbon for low ESR and enhanced energy density supercapacitors, *J. Energy Storage*, 2024, **75**, 109728.

33 L. Cao, H. Li, Z. Xu, H. Zhang, L. Ding, S. Wang, G. Zhang, H. Hou, W. Xu, F. Yang and S. Jiang, Comparison of the heteroatoms-doped biomass-derived carbon prepared by one-step nitrogen-containing activator for high performance supercapacitor, *Diamond Relat. Mater.*, 2021, **114**, 108316.

34 Y. Gogotsi and R. M. Penner, Energy Storage in Nanomaterials – Capacitive, Pseudocapacitive, or Battery-like?, *ACS Nano*, 2018, **12**, 2081–2083.

35 A. Andreyev, M. Akaishi and D. Golberg, Synthesis of nanocrystalline nitrogen-rich carbon nitride powders at high pressure, *Diamond Relat. Mater.*, 2002, **11**, 1885–1889.

36 P. V. Zinin, L.-C. Ming, S. K. Sharma, V. N. Khabashesku, X. Liu, S. Hong, S. Endo and T. Acosta, Ultraviolet and near-infrared Raman spectroscopy of graphitic C_3N_4 phase, *Chem. Phys. Lett.*, 2009, **472**, 69–73.

37 W. Li, D. Peng, W. Huang, X. Zhang, Z. Hou, W. Zhang, B. Lin and Z. Xing, Adjusting coherence length of expanded graphite by self-activation and its electrochemical implication in potassium ion battery, *Carbon*, 2023, **204**, 315–324.

38 W. Li, M. Xiao, J. Jiang, Y. Li, X. Zhang, S. Li, X. Lin, D. Peng, S. W. Or, S. Sun and Z. Xing, Co_4N nanoparticles embedded in N-doped carbon pores: Advanced interlayer material for lithium-sulfur batteries, *Nano Energy*, 2025, **142**, 111140.

39 W. Wu, J. C. Ranasinghe, A. Chatterjee and S. Huang, Recent advances on Raman spectroscopy of graphene: towards biosensing applications, *Mater. Chem. Phys.*, 2024, **318**, 129281.

40 Q. Chen, Y. Zhao, X. Huang, N. Chen and L. Qu, Three-dimensional graphitic carbon nitride functionalized graphene-based high-performance supercapacitors, *J. Mater. Chem. A*, 2015, **3**, 6761–6766.

41 W. Zhu, D. Shen and H. Xie, Combination of chemical activation and nitrogen doping toward hierarchical porous carbon from *houttuynia cordata* for supercapacitors, *J. Energy Storage*, 2023, **60**, 106595.

42 W. Zhu, D. Shen and H. Xie, Effect of Heteroatoms on Pseudocapacitance for N/O Co-doped Porous Carbon in an Alkaline Aqueous Electrolyte, *Energy Fuels*, 2023, **37**, 12467–12473.

43 B. Szubzda, A. Szmaja and A. Halama, Influence of structure and wettability of supercapacitor electrodes carbon materials on their electrochemical properties in water and organic solutions, *Electrochim. Acta*, 2012, **86**, 255–259.

44 G. Lota and E. Frackowiak, Pseudocapacitance Effects for Enhancement of Capacitor Performance, *Fuel Cells*, 2010, **10**, 848–855.

45 Y.-H. Lee, K.-H. Chang and C.-C. Hu, Differentiate the pseudocapacitance and double-layer capacitance contributions for nitrogen-doped reduced graphene oxide in acidic and alkaline electrolytes, *J. Power Sources*, 2013, **227**, 300–308.

46 B.-A. Mei, O. Munteshari, J. Lau, B. Dunn and L. Pilon, Physical Interpretations of Nyquist Plots for EDLC Electrodes and Devices, *J. Phys. Chem. C*, 2018, **122**, 194–206.

47 D. R. Chen, P. K. Adusei, M. Chitranshi, Y. Fang, K. Johnson, M. Schulz and V. Shanov, Electrochemical activation to enhance the volumetric performance of carbon nanotube electrodes, *Appl. Surf. Sci.*, 2021, **541**, 148448.

48 S. N. Faisal, E. Haque, N. Noorbehesht, W. Zhang, A. T. Harris, T. Church and A. I. Minett, Pyridinic and graphitic nitrogen-rich graphene for high-performance supercapacitors and metal-free bifunctional electrocatalysts for ORR and OER, *RSC Adv.*, 2017, **7**, 17950–17958.

49 S. Rajput, V. Tyagi, Sonika, R. Nayak and S. K. Verma, Waste-Derived Activated Carbon for Supercapacitors: Current Trends and Future Prospects, *Energy Technol.*, 2025, **13**, 2401977.

